Multilayered Discrete Green's Functions Based on Mixed-Potential Finite-Difference Formulation

Salma Mirhadi, Mohammad Soleimani, and Ali Abdolali

***Abstract*—An approach to calculating discrete Green's functions (DGFs) in multilayered media is proposed based on the finite-difference scheme of time-domain mixed-potential equations. The calculated DGFs have very high accuracy in comparison to the direct FDTD solution. Furthermore, the steady-state values of the DGFs are properly estimated in terms of the scalar potential, ensuring stability out of the truncating window. These DGFs are applicable to the analysis of antennas with multilayered planar structures. In such analysis, the proposed method has the advantage of the method of moments in that the computations are performed only on the antenna, regardless of the white space around it. Moreover, the broadband frequency characteristic of the antenna is achieved with a single simulation run, such as in the FDTD method. The theoretical results have been verified by the experimental results on a wideband coplanar waveguide (CPW)-fed monopole antenna.**

***Index Terms*—Discrete Green's function, finite-difference time-domain equations, mixed-potential equations, printed antennas.**

I. Introduction

PROMISING features of discrete Green's functions (DGFs) were originally identified by Vazquez and Parini [1], [2]. As opposed to the discretized version of continuous Green's functions, DGFs have attributes consistent with the finite-difference time-domain (FDTD) method, such as dispersion and stability. Thus far, various closed-forms of DGFs in infinite free space have been derived by several authors [1], [3]–[5]. The applications of DGFs have also been investigated in terms of their implementation as absorbing boundary conditions [6]–[8], in FDTD simulations on disjoint domains [9], in the truncation of the FDTD computational grid in the presence of reflecting external media [10], and in terms of savings in runtime and memory usage in radiation and scattering problems [3], [11]–[14].

The analytical closed-form of DGFs includes binomial coefficients, in which the accurate generation of these functions, especially for high upper indices, requires significant processor time due to the necessity of handling multiple precision arithmetic libraries [15], [16]. Nevertheless, closed-form-DGFs return exact values of the FDTD computations in the infinite Yee's mesh with multiple precision arithmetic and do not reflect the numerical error stemming from the finite numerical precision of the FDTD computations in standard arithmetic [16], [17]. However, the extracted analytical DGFs are only for homogenous media, which restricts their application in antenna modeling.

In this paper, a new procedure for extracting the time-domain DGFs in multilayered media is introduced. The proposed method is based on the finite-difference scheme for time-domain mixed-potential equations. This method does not suffer from the drawbacks of analytical closed-form implementation. In [18], the time-domain layered-medium Green's functions for mixed-potential integral equations (MPIE) were established through the fast Hankel transform and fast Fourier transform (FFT) of Green's functions in the complex frequency domain. However, the salient feature of the proposed method is that the solution space is inherently discrete and the equations are in the time-domain. Therefore, the formulation of the problem is much more straightforward than in the method presented in [18]. The calculated DGFs show very high accuracy in comparison to the direct FDTD solution. We have also shown that, in the derivation of multilayered DGFs, the direct implementation of the FDTD has some limitations with regard to the estimation of the steady-state values of DGFs. These steady-state values are required for the truncating window in the convolution calculation.

The proposed method has potential applications in printed antenna modeling. Numerous papers have presented MPIE based on spectral domain Green's functions toward solving printed antennas, [19]–[21]. On the contrary, we have developed mixed-potential finite-difference equations based on time-domain discrete Green's functions. Our proposed method has the advantages of MPIE in that a three-dimensional problem is reduced to a two-dimensional one.

The whole formulation, implementation, and evaluation of the extracted DGFs through the finite-difference scheme of mixed-potential equations are presented in Section II. In Section III, two types of printed antennas are analyzed in the time-domain with the discrete Green's function method, and the computer resources required for the analysis of these antennas are discussed.

II. Formulation

A. Modeling of the Structure

First, a simple case of two dielectric half-spaces, as shown in Fig. 1, is studied. The dielectric in regions 1 and 2 is assumed to be isotropic and lossless with permittivity ϵ_1 and ϵ_2, respectively, and to be infinite in the transverse direction. A y-directed

Manuscript received October 14, 2013; revised July 07, 2014; accepted August 05, 2014. Date of publication August 29, 2014; date of current version October 28, 2014.

The authors are with the Electrical Engineering Department, Iran University of Science and Technology (IUST), Tehran 16846-13114, Iran (e-mail: s_mirhadi@iust.ac.ir; soleimani@iust.ac.ir; abdolali@iust.ac.ir).

Color versions of one or more of the figures in this paper are available online at http://ieeexplore.ieee.org.

Digital Object Identifier 10.1109/TAP.2014.2353654

0018-926X © 2014 IEEE. Personal use is permitted, but republication/redistribution requires IEEE permission.
See http://www.ieee.org/publications_standards/publications/rights/index.html for more information.

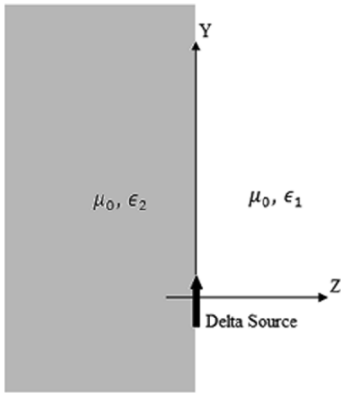

Fig. 1. Geometry of the two dielectric half-spaces with a horizontal current source on the interface.

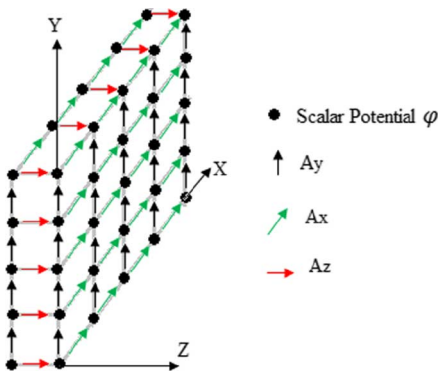

Fig. 2. Scalar and vector potential distribution in the discrete model.

delta current source is located on the dielectric interface. The analytical dyadic spectral domain Green's function can be derived from the solution of the mixed-potential equations. Since we are seeking a discrete time and space solution for the Green's function, the medium is meshed, as shown in Fig. 2. It is modeled as a uniform rectangular lattice, with space increments Δx, Δy, and Δz in the x-, y-, and z-coordinate directions, respectively. The discrete representation of the magnetic vector potential follows the same scheme as the electric field in the Yee's algorithm of the FDTD method, and the intersections of the grid represent the scalar potential. It is important to note that, due to the finite numerical precision, all three components of the magnetic vector potential have nonzero values although the analytical solution shows zero value for A_x.

To establish the discrete Green's functions, the current source at the location (i_s, j_s, k_s) is considered as the following Kronecker delta function:

$$Jy^n_{i_s,j_s,k_s} = \delta^n_{i-i_s,j-j_s,k-k_s}. \tag{1}$$

According to the continuity condition of the electric current, the electric charge can be computed as

$$\rho = -\int \nabla . J dt \tag{2}$$

$$\rho^{n+1/2}_{i,j,k} = -\sum_{\acute{n}=0}^{n} \frac{Jy^{\acute{n}}_{i,j,k} - Jy^{\acute{n}}_{i,j-1,k}}{\Delta y}\Delta t. \tag{3}$$

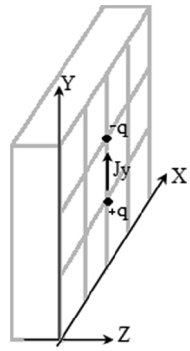

Fig. 3. Current and charges at the interface, $q = -(\Delta t/\Delta y)U^n$.

Substituting (1) into (3) results in

$$q^{n+1/2}_{i_s,j_s+1,k_s} = \frac{\Delta t}{\Delta y}U^n \tag{4}$$

$$q^{n+1/2}_{i_s,j_s,k_s} = -\frac{\Delta t}{\Delta y}U^n \tag{5}$$

where U^n is the unit step discrete function having the value of 1 when $\mathrm{n} \geq 0$. Since the electric charge is obtained in the form of the step function, the scalar potential determines the steady-state values of the DGFs. Fig. 3 shows the current and the related charges at the interface.

B. Scalar Potential

In this section, we determine the expressions of the scalar potential nodes. The scalar homogeneous wave equation is satisfied for the nodes within each dielectric medium, and its corresponding second-order finite-difference representation is of the following form:

$$\begin{aligned}\varphi^{n+1/2}_{i,j,k} =& 2\left(1-\alpha_{x1,2}-\alpha_{y1,2}-\alpha_{z1,2}\right)\varphi^{n-1/2}_{i,j,k} \\ &+ \alpha_{x1,2}\left(\varphi^{n-1/2}_{i+1,j,k}+\varphi^{n-1/2}_{i-1,j,k}\right) \\ &+ \alpha_{y1,2}\left(\varphi^{n-1/2}_{i,j+1,k}+\varphi^{n-1/2}_{i,j-1,k}\right) \\ &+ \alpha_{z1,2}\left(\varphi^{n-1/2}_{i,j,k+1}+\varphi^{n-1/2}_{i,j,k-1}\right) - \varphi^{n-3/2}_{i,j,k}\end{aligned} \tag{6}$$

where $\alpha_{s1,2} = ((\Delta t/\Delta s)(1/\sqrt{\mu\epsilon_{1,2}}))^2$; $s = x, y, z$, and subscripts 1 and 2 refer to media 1 ($k > k_s$) and 2 ($k < k_s$), respectively. Equation (6) should be modified for the nodes on the interface ($k = k_s$). The electric field expression in terms of the potentials is given in (7). By multiplying (7) by ϵ and taking its divergence, we obtain (8)

$$E = -\frac{\partial A}{\partial t} - \nabla\varphi \tag{7}$$

$$\nabla.(\epsilon E) = -\nabla.\left(\epsilon\frac{\partial A}{\partial t}\right) - \nabla.(\epsilon\nabla\varphi). \tag{8}$$

By applying the Lorentz gauge in the nonhomogeneous media as

$$\mu\epsilon\frac{\partial\varphi}{\partial t} = -\frac{1}{\epsilon}\nabla.(\epsilon A) \tag{9}$$

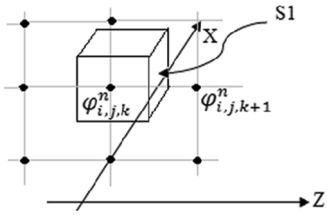

Fig. 4. Integration cube of (11).

we obtain

$$\nabla.(\epsilon E) = \mu\epsilon^2 \frac{\partial^2 \varphi}{\partial t^2} - \nabla.(\epsilon \nabla \varphi). \tag{10}$$

Integrating over a cube with side lengths of Δx, Δy, and Δz around a node on the interface and applying the divergence theorem yield the following result:

$$\int_{\mathrm{v}} q\, dv = \int_{\mathrm{v}} \mu\epsilon^2 \frac{\partial^2 \varphi}{\partial t^2} dv - \int_s (\epsilon \nabla \varphi).ds. \tag{11}$$

S is the entire enclosed surface of the cube. The expression of $\nabla\varphi$ on each side of the cube can be evaluated from the adjacent nodes. As an example, $\nabla\varphi$ is calculated for the S_1 of Fig. 4 as

$$\int_{s_1} (\epsilon \nabla \varphi).ds = \epsilon_1 \frac{\varphi^{n-1/2}_{i,j,k+1} - \varphi^{n-1/2}_{i,j,k}}{\Delta Z} \Delta x \Delta y. \tag{12}$$

The effective dielectric constant assigned to the cells on the interface is the average value of dielectric constants, $\epsilon_{avg} = (\epsilon_1 + \epsilon_2)/2$. Equation (11) can thus be written as

$$\begin{aligned} & q^{n-1/2}_{i,j,k} \Delta x \Delta y \Delta z \\ &= \mu\epsilon^2_{avg} \frac{\varphi^{n+1/2}_{i,j,k} - 2\varphi^{n-1/2}_{i,j,k} + \varphi^{n-3/2}_{i,j,k}}{\Delta t^2} \Delta x \Delta y \Delta z \\ &\quad - \left\{ \epsilon_1 \frac{\varphi^{n-1/2}_{i,j,k+1} - \varphi^{n-1/2}_{i,j,k}}{\Delta z} - \epsilon_2 \frac{\varphi^{n-1/2}_{i,j,k} - \varphi^{n-1/2}_{i,j,k-1}}{\Delta z} \right\} \Delta x \Delta y \\ &\quad - \epsilon_{avg} \left\{ \frac{\varphi^{n-1/2}_{i,j+1,k} - \varphi^{n-1/2}_{i,j,k}}{\Delta y} - \frac{\varphi^{n-1/2}_{i,j,k} - \varphi^{n-1/2}_{i,j-1,k}}{\Delta y} \right\} \Delta x \Delta z \\ &\quad - \epsilon_{avg} \left\{ \frac{\varphi^{n-1/2}_{i+1,j,k} - \varphi^{n-1/2}_{i,j,k}}{\Delta x} - \frac{\varphi^{n-1/2}_{i,j,k} - \varphi^{n-1/2}_{i-1,j,k}}{\Delta x} \right\} \Delta x \Delta z. \end{aligned} \tag{13}$$

Rearranging (13), we obtain

$$\begin{aligned} & \varphi^{n+1/2}_{i,j,k_s} \\ &= q^{n-1/2}_{i,j,k} \frac{\Delta t^2}{\mu\epsilon^2_{avg}} + 2\left(1 - \alpha_{x3} - \alpha_{y3} - \alpha_{z3}\right) \varphi^{n-1/2}_{i,j,k} \\ &\quad + \alpha_{x3} \left(\varphi^{n-1/2}_{i+1,j,k} + \varphi^{n-1/2}_{i-1,j,k} \right) + \alpha_{y3} \left(\varphi^{n-1/2}_{i,j+1,k} + \varphi^{n-1/2}_{i,j-1,k} \right) \\ &\quad + \alpha_{z3} \left(\frac{\epsilon_1}{\epsilon_{avg}} \varphi^{n-1/2}_{i,j,k+1} + \frac{\epsilon_2}{\epsilon_{avg}} \varphi^{n-1/2}_{i,j,k-1} \right) - \varphi^{n-3/2}_{i,j,k} \end{aligned} \tag{14}$$

where $\alpha_{s3} = ((\Delta t/\Delta s)(1/\sqrt{\mu\epsilon_{avg}}))^2$; $s = x, y, z$.

C. Magnetic Vector Potential

To establish finite-difference equations for the magnetic vector potential, its spatial components are divided into two categories: the components that exist on the boundary (A_x and A_y) and the component that does not exist on the boundary (A_z).

For the first category, similarly to (6), the scalar homogeneous wave equation is satisfied for the nodes that are inside each dielectric medium, as shown in (15)

$$\begin{aligned} A_{x,y}{}^{n+1}_{i,j,k} &= 2(1 - \alpha_{x1,2} - \alpha_{y1,2} - \alpha_{z1,2}) A_{x,y}{}^{n}_{i,j,k} \\ &\quad + \alpha_{x1,2} \left(A_{x,y}{}^{n}_{i+1,j,k} + A_{x,y}{}^{n}_{i-1,j,k} \right) \\ &\quad + \alpha_{y1,2} \left(A_{x,y}{}^{n}_{i,j+1,k} + A_{x,y}{}^{n}_{i,j-1,k} \right) \\ &\quad + \alpha_{z1,2} \left(A_{x,y}{}^{n}_{i,j,k+1} + A_{x,y}{}^{n}_{i,j,k-1} \right) - A_{x,y}{}^{n-1}_{i,j,k} \end{aligned} \tag{15}$$

Modification is required for the interface grid points. The general form of the wave equation for the magnetic potential is expressed as

$$\mu\epsilon_{avg} \frac{\partial^2 A_x}{\partial t^2} = -\mu\epsilon_{avg} \frac{\partial^2 \varphi}{\partial t \partial x} - (\nabla \times \nabla \times A)_x \tag{16}$$

$$\mu\epsilon_{avg} \frac{\partial^2 A_y}{\partial t^2} = \mu J_y - \mu\epsilon_{avg} \frac{\partial^2 \varphi}{\partial t \partial y} - (\nabla \times \nabla \times A)_y. \tag{17}$$

The finite-difference form of the nonhomogeneous Lorentz gauge in (9) is, on the boundary,

$$\begin{aligned} -\mu\epsilon_{avg} \frac{\varphi^{n+1/2}_{i,j,k} - \varphi^{n-1/2}_{i,j,k}}{\Delta t} &= \frac{A_{x}{}^{n}_{i,j,k} - A_{x}{}^{n}_{i-1,j,k}}{\Delta x} \\ &\quad + \frac{A_{y}{}^{n}_{i,j,k} - A_{x}{}^{n}_{i,j-1,k}}{\Delta y} \\ &\quad + \frac{\epsilon_1 A_{z}{}^{n}_{i,j,k} - \epsilon_2 A_{z}{}^{n}_{i,j,k-1}}{\epsilon_{avg} \Delta z}. \end{aligned} \tag{18}$$

By taking the derivative of (18) with respect to x (and y) and substituting its value into (16) (and (17)), we obtain

$$\begin{aligned} A_{x}{}^{n+1}_{i,j,k} &= 2(1 - \alpha_{x3} - \alpha_{y3} - \alpha_{z3}) A_{x}{}^{n}_{i,j,k} \\ &\quad + \alpha_{x3} \left(A_{x}{}^{n}_{i+1,j,k} + A_{x}{}^{n}_{i-1,j,k} \right) \\ &\quad + \alpha_{y3} \left(A_{x}{}^{n}_{i,j+1,k} + A_{x}{}^{n}_{i,j-1,k} \right) \\ &\quad + \sqrt{\alpha_{x3}\alpha_{z3}} \left(\frac{\epsilon_1}{\epsilon_{avg}} - 1 \right) \left(A_{z}{}^{n}_{i+1,j,k} - A_{z}{}^{n}_{i,j,k} \right) \\ &\quad + \sqrt{\alpha_{x3}\alpha_{z3}} \left(\frac{\epsilon_2}{\epsilon_{avg}} - 1 \right) \left(A_{z}{}^{n}_{i+1,j,k-1} - A_{z}{}^{n}_{i,j,k-1} \right) \\ &\quad - A_{x}{}^{n-1}_{i,j,k}, \end{aligned} \tag{19}$$

$$\begin{aligned} A_{y}{}^{n+1}_{i,j,k} &= \frac{\Delta t^2}{\epsilon_{avg}} J_{y}{}^{n}_{i,j,k} + 2(1 - \alpha_{x3} - \alpha_{y3} - \alpha_{z3}) A_{y}{}^{n}_{i,j,k} \\ &\quad + \alpha_{x3} \left(A_{y}{}^{n}_{i+1,j,k} + A_{y}{}^{n}_{i-1,j,k} \right) \\ &\quad + \alpha_{y3} \left(A_{y}{}^{n}_{i,j+1,k} + A_{y}{}^{n}_{i,j-1,k} \right) \\ &\quad + \sqrt{\alpha_{y3}\alpha_{z3}} \left(\frac{\epsilon_1}{\epsilon_{avg}} - 1 \right) \left(A_{z}{}^{n}_{i,j+1,k} - A_{z}{}^{n}_{i,j,k} \right) \\ &\quad + \sqrt{\alpha_{y3}\alpha_{z3}} \left(\frac{\epsilon_2}{\epsilon_{avg}} - 1 \right) \left(A_{z}{}^{n}_{i,j+1,k-1} - A_{z}{}^{n}_{i,j,k-1} \right) \\ &\quad - A_{y}{}^{n-1}_{i,j,k}. \end{aligned} \tag{20}$$

For the second category, since A_z does not have any nodes on the interface, the finite-difference scalar homogeneous wave equation is satisfied for all nodes. However, it always gives a zero answer. Therefore, we have to apply the general form of the wave equation for the nodes adjacent to the interface, given as

$$\mu\epsilon_{1,2}\frac{\partial^2 A_z}{\partial t^2} = -\mu\epsilon_{1,2}\frac{\partial^2 \varphi}{\partial t \partial z} - (\nabla \times \nabla \times A)_z \tag{21}$$

with the following finite-difference representation:

$$\begin{aligned} {A_z}_{i,j,k}^{n+1} =& 2(1-\alpha_{x1,2}-\alpha_{y1,2}){A_z}_{i,j,k}^{n} + \alpha_{x1,2}\left({A_z}_{i+1,j,k}^{n} \right. \\ &\left. + {A_z}_{i-1,j,k}^{n}\right) + \alpha_{y1,2}\left({A_z}_{i,j+1,k}^{n} + {A_z}_{i,j-1,k}^{n}\right) \\ &- \frac{\Delta t}{\Delta z}\left(\varphi_{i,j,k+1}^{n+1/2} - \varphi_{i,j,k+1}^{n-1/2} - \varphi_{i,j,k}^{n+1/2} + \varphi_{i,j,k}^{n-1/2}\right) \\ &- \sqrt{\alpha_{x1,2}\alpha_{z1,2}}\left({A_x}_{i,j,k+1}^{n} - {A_x}_{i-1,j,k+1}^{n} - {A_x}_{i,j,k}^{n} \right. \\ &\left. + {A_x}_{i-1,j,k}^{n}\right) \\ &- \sqrt{\alpha_{y1,2}\alpha_{z1,2}}\left({A_y}_{i,j,k+1}^{n} - {A_y}_{i,j-1,k+1}^{n} - {A_y}_{i,j,k}^{n} \right. \\ &\left. + {A_y}_{i,j-1,k}^{n}\right) - {A_z}_{i,j,k}^{n-1} \end{aligned} \tag{22}$$

where subscripts 1 and 2 refer to the nodes inside media 1 ($k = k_s$) and 2 ($k = k_s - 1$), respectively. For the rest of the nodes, we use the following finite-difference scalar homogeneous wave equation:

$$\begin{aligned} {A_z}_{i,j,k}^{n+1} =& 2(1-\alpha_{x1,2}-\alpha_{y1,2}-\alpha_{z1,2}){A_z}_{i,j,k}^{n} \\ &+ \alpha_{x1,2}\left({A_z}_{i+1,j,k}^{n} + {A_z}_{i-1,j,k}^{n}\right) \\ &+ \alpha_{y1,2}\left({A_z}_{i,j+1,k}^{n} + {A_z}_{i,j-1,k}^{n}\right) \\ &+ \alpha_{z1,2}\left({A_z}_{i,j,k+1}^{n} + {A_z}_{i,j,k-1}^{n}\right) - {A_z}_{i,j,k}^{n-1}. \end{aligned} \tag{23}$$

The finite-difference form of the electric fields can be expressed in terms of the potentials as

$${E_x}_{i,j,k}^{n+1/2} = \left({A_x}_{i,j,k}^{n+1} - {A_x}_{i,j,k}^{n}\right)/\Delta t - \left(\varphi_{i+1,j,k}^{n+1/2} - \varphi_{i,j,k}^{n+1/2}\right)/\Delta x \tag{24}$$

$${E_y}_{i,j,k}^{n+1/2} = \left({A_y}_{i,j,k}^{n+1} - {A_y}_{i,j,k}^{n}\right)/\Delta t - \left(\varphi_{i,j+1,k}^{n+1/2} - \varphi_{i,j,k}^{n+1/2}\right)/\Delta y \tag{25}$$

$${E_z}_{i,j,k}^{n+1/2} = \left({A_z}_{i,j,k}^{n+1} - {A_z}_{i,j,k}^{n}\right)/\Delta t - \left(\varphi_{i,j,k+1}^{n+1/2} - \varphi_{i,j,k}^{n+1/2}\right)/\Delta z. \tag{26}$$

D. Implementation for Multilayered Media

The previous formulation can be extended to multilayered structures. Fig. 5(a) shows a multilayered medium with $n+1$ dielectric layers and n interfaces located at k_i, $i = 1, \ldots, n$. The medium is assumed to be infinite in the transverse direction. A y-directed delta current source is located at (i_s, j_s, k_s) on the k_s-th interface. The Δz increment is selected such that the A_x, A_y, and φ nodes are located on the interfaces, as in the Y-X plane in Fig. 2. In this manner, the update equations for the scalar and vector potentials inside each layer are given by

$$\begin{aligned} \varphi_{i,j,k}^{n+1/2} =& 2(1-\alpha_{xm}-\alpha_{ym}-\alpha_{zm})\varphi_{i,j,k}^{n-1/2} \\ &+ \alpha_{xm}\left(\varphi_{i+1,j,k}^{n-1/2} + \varphi_{i-1,j,k}^{n-1/2}\right) \\ &+ \alpha_{ym}\left(\varphi_{i,j+1,k}^{n-1/2} + \varphi_{i,j-1,k}^{n-1/2}\right) \\ &+ \alpha_{zm}\left(\varphi_{i,j,k+1}^{n-1/2} + \varphi_{i,j,k-1}^{n-1/2}\right) - \varphi_{i,j,k}^{n-3/2} \end{aligned} \tag{27}$$

$$\begin{aligned} {A_s}_{i,j,k}^{n+1} =& 2(1-\alpha_{xm}-\alpha_{ym}-\alpha_{zm}){A_s}_{i,j,k}^{n} \\ &+ \alpha_{xm}\left({A_s}_{i+1,j,k}^{n} + {A_s}_{i-1,j,k}^{n}\right) \\ &+ \alpha_{ym}\left({A_s}_{i,j+1,k}^{n} + {A_s}_{i,j-1,k}^{n}\right) \\ &+ \alpha_{zm}\left({A_s}_{i,j,k+1}^{n} + {A_x,y}_{i,j,k-1}^{n}\right) \\ &- {A_s}_{i,j,k}^{n-1}; \quad s = x, y, z. \end{aligned} \tag{28}$$

where $\alpha_{sm} = ((\Delta t/\Delta s)(1/\sqrt{\mu\epsilon_m}))^2$; $s = x, y, z$. The update equations for φ, A_x, and A_y on the m-th interface are given by

$$\begin{aligned} \varphi_{i,j,k_m}^{n+1/2} =& 2(1-\alpha_{xma}-\alpha_{yma}-\alpha_{zma})\varphi_{i,j,k}^{n-1/2} \\ &+ \alpha_{xma}\left(\varphi_{i+1,j,k}^{n-1/2} + \varphi_{i-1,j,k}^{n-1/2}\right) \\ &+ \alpha_{yma}\left(\varphi_{i,j+1,k}^{n-1/2} + \varphi_{i,j-1,k}^{n-1/2}\right) \\ &+ \alpha_{zma}\left(\frac{\epsilon_{m+1}}{\epsilon_{m\_avg}}\varphi_{i,j,k+1}^{n-1/2} + \frac{\epsilon_m}{\epsilon_{m\_avg}}\varphi_{i,j,k-1}^{n-1/2}\right) \\ &- \varphi_{i,j,k}^{n-3/2} \end{aligned} \tag{29}$$

$$\begin{aligned} {A_x}_{i,j,k_m}^{n+1} =& 2(1-\alpha_{xma}-\alpha_{yma}-\alpha_{zma}){A_x}_{i,j,k}^{n} \\ &+ \alpha_{xma}\left({A_x}_{i+1,j,k}^{n} + {A_x}_{i-1,j,k}^{n}\right) \\ &+ \alpha_{yma}\left({A_x}_{i,j+1,k}^{n} + {A_x}_{i,j-1,k}^{n}\right) \\ &+ \sqrt{\alpha_{xma}\alpha_{zma}}\left(\left(\frac{\epsilon_{m+1}}{\epsilon_{m_{avg}}} - 1\right)\left({A_z}_{i+1,j,k}^{n} - {A_z}_{i,j,k}^{n}\right)\right. \\ &\left. + \left(\frac{\epsilon_m}{\epsilon_{m_{avg}}} - 1\right)\left({A_z}_{i+1,j,k-1}^{n} - {A_z}_{i,j,k-1}^{n}\right)\right) - {A_x}_{i,j,k}^{n-1} \end{aligned} \tag{30}$$

$$\begin{aligned} {A_y}_{i,j,k_m}^{n+1} =& 2(1-\alpha_{xma}-\alpha_{yma}-\alpha_{zma}){A_y}_{i,j,k}^{n} \\ &+ \alpha_{xma}\left({A_y}_{i+1,j,k}^{n} + {A_y}_{i-1,j,k}^{n}\right) \\ &+ \alpha_{yma}\left({A_y}_{i,j+1,k}^{n} + {A_y}_{i,j-1,k}^{n}\right) \\ &+ \sqrt{\alpha_{yma}\alpha_{zma}}\left(\left(\frac{\epsilon_{m+1}}{\epsilon_{m_{avg}}} - 1\right)\left({A_z}_{i,j+1,k}^{n} - {A_z}_{i,j,k}^{n}\right)\right. \\ &\left. + \left(\frac{\epsilon_m}{\epsilon_{m_{avg}}} - 1\right)\left({A_z}_{i,j+1,k-1}^{n} - {A_z}_{i,j,k-1}^{n}\right)\right) - {A_y}_{i,j,k}^{n-1} \end{aligned} \tag{31}$$

where $\alpha_{sma} = ((\Delta t/\Delta s)(1/\sqrt{\mu\epsilon_{m\_avg}}))^2$; $s = x, y, z$ and $\epsilon_{m\_avg} = (\epsilon_m + \epsilon_{m+1})/2$. For the k_s-th interface at the location of the source, the term $q_{i,j,k}^{n-1/2}\Delta t^2/\mu\epsilon_{m\_avg}^2$ related to the charges and the term $J_{y_{i,j,k}}^{n}\Delta t^2/\epsilon_{m\_avg}$ related to the current source are added to (29) and (31), respectively. As previously mentioned, for the nodes adjacent to the interface, the update equation of (28) for the A_z component is replaced with (32) and (33) as follows:

$$\begin{aligned} {A_z}_{i,j,k_{m-1}}^{n+1} =& 2(1-\alpha_{xm-1}-\alpha_{ym-1}){A_z}_{i,j,k}^{n} \\ &+ \alpha_{xm-1}\left({A_z}_{i+1,j,k}^{n} + {A_z}_{i-1,j,k}^{n}\right) \\ &+ \alpha_{ym-1}\left({A_z}_{i,j+1,k}^{n} + {A_z}_{i,j-1,k}^{n}\right) \\ &- \frac{\Delta t}{\Delta z}\left(\varphi_{i,j,k+1}^{n+1/2} - \varphi_{i,j,k+1}^{n-1/2} - \varphi_{i,j,k}^{n+1/2} + \varphi_{i,j,k}^{n-1/2}\right) \\ &- \sqrt{\alpha_{xm-1}\alpha_{zm-1}}\left({A_x}_{i,j,k+1}^{n} - {A_x}_{i-1,j,k+1}^{n} \right. \\ &\left. - {A_x}_{i,j,k}^{n} + {A_x}_{i-1,j,k}^{n}\right) \\ &- \sqrt{\alpha_{ym-1}\alpha_{zm-1}}\left({A_y}_{i,j,k+1}^{n} - {A_y}_{i,j-1,k+1}^{n} \right. \\ &\left. - {A_y}_{i,j,k}^{n} + {A_y}_{i,j-1,k}^{n}\right) \\ &- {A_z}_{i,j,k}^{n-1} \end{aligned} \tag{32}$$

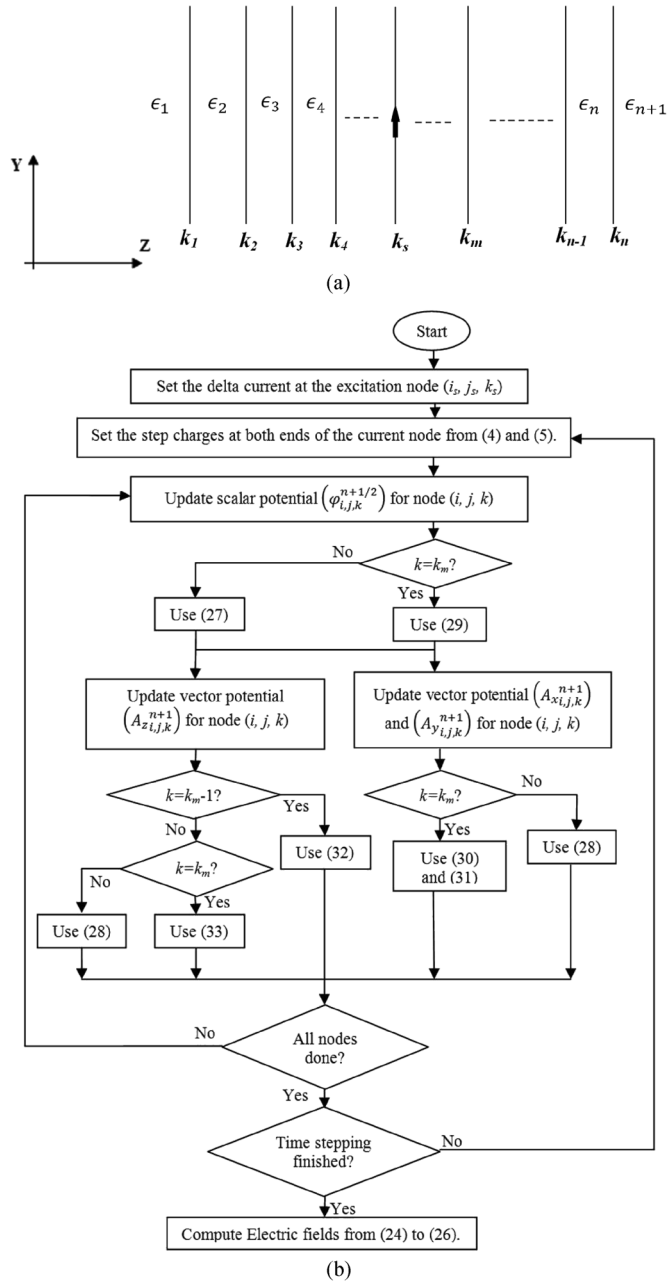

Fig. 5. (a) Geometry of a multilayered medium with a delta current source located at the k_s-th interface, (b) Implementation flowchart of the proposed method for extracting multilayered DGFs.

$$
\begin{aligned}
A_{z}{}_{i,j,k_m}^{n+1} &= 2(1-\alpha_{xm}-\alpha_{ym})A_{z}{}_{i,j,k}^{n} \\
&\quad + \alpha_{xm}\left(A_{z}{}_{i+1,j,k}^{n} + A_{z}{}_{i-1,j,k}^{n}\right) \\
&\quad + \alpha_{ym}\left(A_{z}{}_{i,j+1,k}^{n} + A_{z}{}_{i,j-1,k}^{n}\right) \\
&\quad - \frac{\Delta t}{\Delta z}\left(\varphi_{i,j,k+1}^{n+1/2} - \varphi_{i,j,k+1}^{n-1/2} - \varphi_{i,j,k}^{n+1/2} + \varphi_{i,j,k}^{n-1/2}\right) \\
&\quad - \sqrt{\alpha_{xm}\alpha_{zm}}\left(A_{x}{}_{i,j,k+1}^{n} - A_{x}{}_{i-1,j,k+1}^{n}\right. \\
&\qquad \left. - A_{x}{}_{i,j,k}^{n} + A_{x}{}_{i-1,j,k}^{n}\right) \\
&\quad - \sqrt{\alpha_{ym}\alpha_{zm}}\left(A_{y}{}_{i,j,k+1}^{n} - A_{y}{}_{i,j-1,k+1}^{n}\right. \\
&\qquad \left. - A_{y}{}_{i,j,k}^{n} + A_{y}{}_{i,j-1,k}^{n}\right) \\
&\quad - A_{z}{}_{i,j,k}^{n-1}. \qquad (33)
\end{aligned}
$$

TABLE I
COMPARISON OF THE FDTD METHOD AND THE PROPOSED METHOD FOR G_{yy} CALCULATION

Time Step (n)	FDTD Method	Proposed Method
1	-0.058904862254809	-0.058904862254809
5	-0.016032769375664	-0.016032769375664
10	-0.015992343627958	-0.015992343627958
15	-0.020421507849039	-0.020421507849039
20	-0.021472703294321	-0.021472703294321
30	-0.020483115704992	-0.020483115704988

TABLE II
COMPARISON OF THE FDTD METHOD AND THE PROPOSED METHOD FOR G_{yx} CALCULATION

Time Step (n)	FDTD Method	Proposed Method
1	0	0
5	-0.004367914441089	-0.004367914441089
10	-0.006382794194993	-0.006382794194993
15	-0.006671162847542	-0.006671162847542
20	-0.006621264701012	-0.006621264701012
30	-0.007033465601519	-0.007033465601519

The flowchart in Fig. 5(b) depicts the implementation steps for extracting multilayered DGFs from the finite-difference formulation of mixed-potential equations. Absorbing boundary conditions are not considered here due, on one hand, to the deficiency of the perfectly matched layer (PML) in the proper absorption of the wave that is generated by the delta source with infinite frequency bandwidth and, on the other hand, to the limited number of iterations often required for calculations.

E. Evaluation of the Extracted Multilayered DGFs

The previously obtained discrete Green's functions for the half-space problem are compared with the direct implementation of the Yee's FDTD algorithm. The Δx, Δy, and Δz in the computational domain are taken as 0.5 mm, and the dielectric constants of media 1 and 2 are selected as 1 and 2.2, respectively. The time increment Δt is determined according to the Courant stability condition as $\Delta t = 0.5\,\Delta x/c$, where c is the speed of light. A large spatial grid of $400 \times 400 \times 400$ cells is considered such that the reflected waves from the PML do not reach the observation point in the FDTD simulation. The same spatial grid is also assumed for the computational domain of the mixed-potential method. The y-directed delta current is located on the interface at the center of the grid (in cell position $(i_s, j_s, k_s) = (200, 200, 200)$). The y and x components of the electric field (G_{yy} and G_{yx}, respectively) at the excitation point are listed in Tables I and II. For G_{yy}, the difference lies in the fourteenth decimal place, whereas for G_{yx}, the results are identical to fifteen decimal places. Furthermore, a y-directed point current source with a differentiated Gaussian waveform on the interface of the dielectric is considered, and the electric fields in the x and y directions are obtained by using the convolution of the source (J_y) with G_{yx} and G_{yy}, respectively. The results are compared with those of the FDTD method. The relative error between the results of the FDTD method (X_{ref}^n) and those of the proposed method (X^n) is defined as

$$
\text{Error} = 20\log_{10}\left[\frac{\left|X^n - X_{ref}^n\right|}{\left|X_{ref}^n\right|}\right] \quad (\text{dB}) \qquad (34)
$$

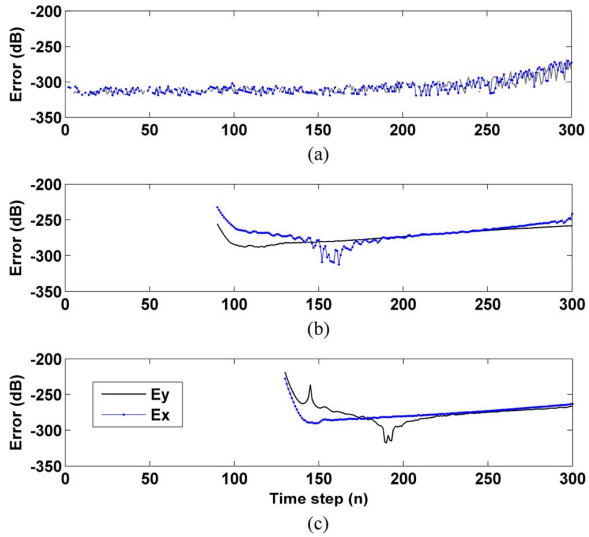

Fig. 6. Relative error between the E_x and E_y waveforms computed using the convolution of the current source with the DGFs and the FDTD method for the cell positions (a) (i_s, j_s, k_s), (b) (i_s, j_s+50, k_s), and (c) (i_s+50, j_s+50, k_s).

which is shown in Fig. 6 for the cell positions (i_s, j_s, k_s), $(i_s, j_s + 50, k_s)$, and $(i_s + 50, j_s + 50, k_s)$. An error below -250 dB is obtained for the computation in double floating-point precision.

The accuracy of the extracted DGFs for multilayered structures is evaluated by using a sample five-layered medium, as shown in Fig. 7(a). The Δx, Δy, and Δz are selected as 0.4 mm, and the y-directed delta current source is located on the interface of media 2 and 3. Fig. 7 shows the relative error between the DGFs computed through the FDTD method and those obtained with the proposed method at three different observation points. As shown in the figure, the accuracy obtained is between -100 dB to -300 dB, which is almost the same as in the half-space problem.

III. Application of Multilayered DGFs in Printed Antennas Modeling

As a practical application of multilayered DGFs, two printed antennas on a dielectric substrate are studied in this section. First, the DGFs of the dielectric substrate are computed by using the flowchart in Fig. 5(b), and those that are on the surface of the antenna are saved. This process is run only once for the given values of the Courant numbers. A nonuniform mesh grid can also be used to model a thin substrate as accurately as the FDTD method. The march-on-in-time scheme of the update equation of the current on the antenna, extracted in [2], [3], is then applied as

$$[\vec{J}]^n_{i,j,k} = \frac{\varepsilon_{avg}}{\Delta t}[\vec{E}_{inc}]^{n+1/2}_{i,j,k} + \frac{\varepsilon_{avg}}{\Delta t}\sum_{n'=0i'}^{n-1}\sum_{j',k'}[\overline{G}]^{n-n'}_{i-i',j-j',k-k'}[\vec{J}]^{n'}_{i',j',k'}$$
$$i, j, k, i', j', k' \text{ on the antenna.} \quad (35)$$

This step can be done for different antenna sizes by using the stored DGFs. Furthermore, this calculation is performed only on the surface of the antenna, regardless of the white space around it.

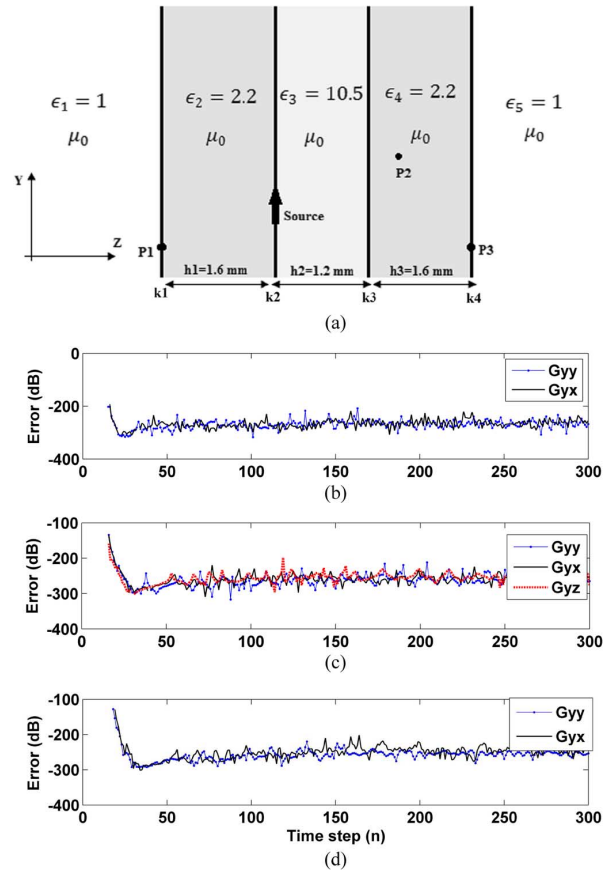

Fig. 7. (a) Geometry of a five-layered medium with a y-directed delta current source on the interface of the media 2 and 3 located at (i_s, j_s, k_2). Relative error between the results of the FDTD method and the proposed method (b) for the P1 point located at $(i_s, j_s - 10, k_1)$, (c) for the P2 point located at $(i_s, j_s + 10, k_3 + 1)$, and (d) for the P3 point located at $(i_s, j_s - 10, k_4)$.

A. Modeling of a Printed Dipole

A simple dipole antenna, printed on a dielectric substrate with the dielectric constant $\epsilon_1 = 2.2$ and thickness $\mathrm{h} = 2$ mm, is shown in Fig. 8. The spatial and time increments are considered as $\Delta x = \Delta y = \Delta z = 0.25$ mm and $c\Delta t = 0.5\Delta x$, respectively. The size of the antenna is selected as $\mathrm{w} = 3$ mm and $\mathrm{L} = 14.5$ mm, with a gap of 0.5 mm between the two arms. First, the DGFs for the infinite substrate are extracted according to the proposed approach, and those that are on the interface of the dielectric are saved. Then, the antenna is excited with the first-order derivative of the Gaussian pulse in the x direction, and the time-domain current is calculated based on (35). The spatial fast Fourier transform is also used to accelerate the calculation of multidimensional convolutions of (35) [22]. As the time step increases, DGFs tend toward nonzero constant values; therefore, by performing appropriate time windowing, the time convolution of the current can be calculated only for N_g time steps instead of for all previous time steps. More accurate results can be obtained by using a Hann window [17]; however, in this case a simple rectangular window function is selected, as follows:

$$W^n = \begin{cases} 0 & n < n_i \\ 1 & n_i < n < n_t \\ constant & n > n_t \end{cases} \quad (36)$$

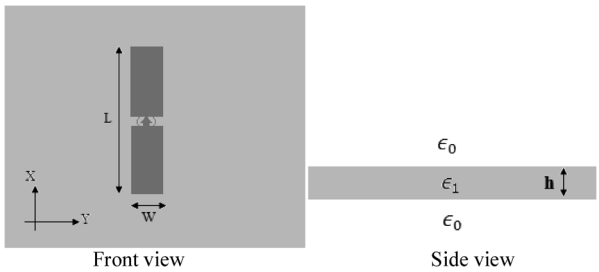

Fig. 8. Geometry of the printed dipole.

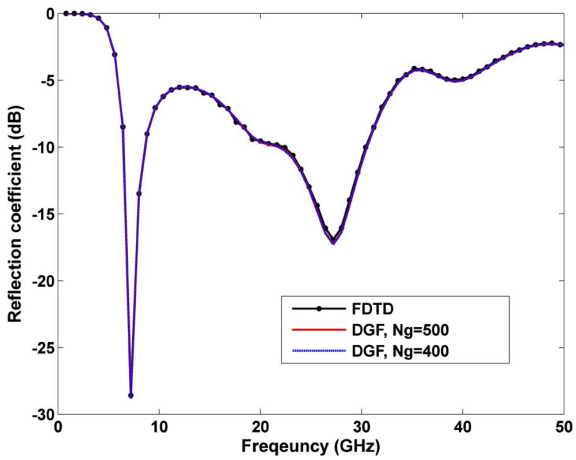

Fig. 9. Simulated return loss of the printed dipole.

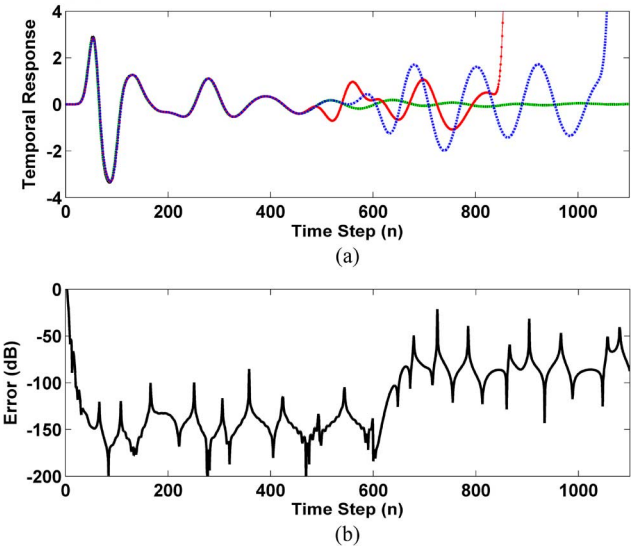

Fig. 10. (a) Comparison of current at the feed location of the printed dipole antenna using the direct FDTD method (black solid line), implementation of (35) when the DGFs are calculated through the proposed mixed-potential method referred to as the DGF method (green dashed line), and implementation of (35) when the DGFs are calculated through the FDTD method with $Ng = 400$ (red line with round marker) and $Ng = 500$ (blue dotted line). (b) Relative error between the current calculated using the direct FDTD method and that obtained with the DGF method.

where n_i is the time step at which the excitation arrives at the calculation point. The window size is $N_g = n_t - n_i$. The constant values outside the window, which play an important role in the stability of the solution, are the steady-state values of the DGFs. As previously mentioned, these are dependent on the scalar potential response, which is not separable in the direct FDTD solution.

In Fig. 9 the frequency response of the printed dipole antenna is shown in comparison with the FDTD method. The window size is selected as $N_g = 400$ and 500. As shown in Fig. 9, a further increase in the window size does not change the simulation results significantly. In addition, the results of the DGF and direct FDTD methods overlap well.

One approach to extracting DGFs is the use of the conventional FDTD method. For this purpose, the electric current source is considered as the Kronecker delta function, and the fields are computed through the update equations of the Yee's algorithm. The required fields are saved as DGFs and applied within (35). However, for ease in the convolution calculations of (35), we have to use windowing, and we need the steady-state values of the DGFs. We cannot consider the DGFs outside the window as zero values because of the existence of the step charges. In the FDTD implementation, the field responses to the charges and the current are not separable. Therefore, the conventional FDTD method for extraction of DGFs cannot estimate the steady-state values of DGFs correctly.

Fig. 10(a) shows the current at the feed location using the direct FDTD method, the implementation of (35) in which DGFs are calculated through the proposed finite-difference solution of the mixed-potential equations (DGF method), and the implementation of (35) in which DGFs are calculated through the FDTD method with $N_g = 400$ and 500. As shown in the figure, the instability of the current out of the window is clear when DGFs are calculated by using the conventional FDTD method. The error between the feed current from the direct FDTD method and that from the DGF method is shown in Fig. 10(b). In the FDTD method, the current of the antenna is obtained by applying Ampere's law. In this way, the current at a certain time instant is dependent on the magnetic field at the same time instant, which in turn is dependent on the electric field at the previous time instant. In contrast, in the DGF method, the current is dependent on the electric field in the future ($E^{n+1/2}$ in (35)). In fact, the current calculation in the FDTD method is a forward solution, whereas the current calculation in the DGF method is an inverse solution. Therefore, a few time steps are needed to adapt the solutions in the initial time steps, and the error never goes below -200 dB in the whole interval. Furthermore, the windowing in DGF simulation and the reflections from the absorbing boundary conditions in FDTD simulation lead to an error below -50 dB at the end of the interval, at which the values of the current are smaller and more sensitive to numerical computations.

B. Modeling of a CPW-Fed Monopole Antenna

As another example, a rectangular monopole antenna with a coplanar waveguide (CPW) feed is studied. The antenna, shown in Fig. 11, is printed on an FR4 substrate with thickness of 1.6 mm, relative permittivity of 4.4, and loss tangent of 0.02. The spatial and time increments are set to $\Delta x = \Delta y = \Delta z = 0.2$ mm and $c\Delta t = 0.5\Delta x$, respectively. The total number of cells is 100×83, corresponding to the x and y directions. As depicted in Fig. 12, the x-directed incident electric fields are between the central strip and the ground planes and are 180° out of

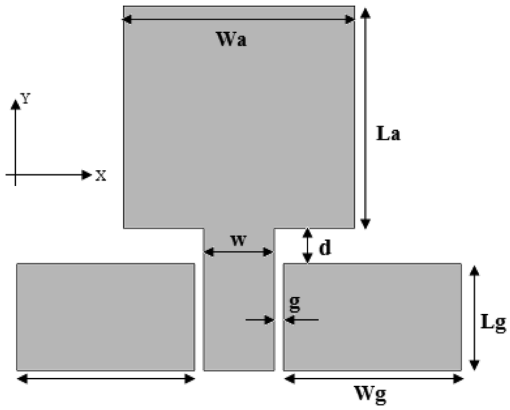

Fig. 11. Geometry of a CPW-fed rectangular monopole antenna with La = 10 mm, Wa = 10.4 mm, Lg = 4.8 mm, Wg = 8 mm, w = 3.2 mm, g = 0.4 mm, and d = 1.6 mm.

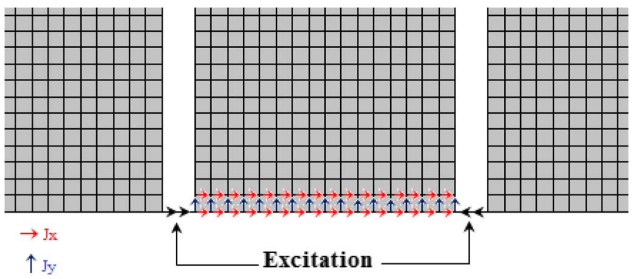

Fig. 12. A portion of the mesh grid showing the excitation and current distribution. The relative positions of the electric currents follow the same distributions as the electric fields in the Yee's grid.

phase in the two slots from which the CPW is excited in the even mode. After launching the first derivative Gaussian pulse excitation, the transient currents are computed at successive time steps by using (35). Then, the input impedance of the antenna can be determined by using the voltage and the current, which are defined as follows:

$$V_n = \Delta x \; n_{xslot} \frac{E^{n+1/2}_{xinc} + E^{n-1/2}_{xinc}}{2} \tag{37}$$

$$I^n = \Delta x \Delta z \sum\nolimits_i J^n_{y\,i,j=1}; \text{i on the center conductor} \tag{38}$$

where n_{xslot} is the number of nodes in the slot (in this case, 2). Fig. 13 shows the reflection coefficient measurement and simulation results, which are in reasonable agreement. The omission of the dielectric losses and antenna thickness in the simulations may account for the difference between the simulated and measured results.

C. Computer Resources

In this section, we present some information on computer resources to facilitate further research on the proposed method. All computations in this study were carried out on a 64-bit PC with an 8-core 3.5 GHz CPU and 32 GB RAM. The codes were written in FORTRAN, in which the numbers were represented by double floating-point precision. The written codes were compiled on a single CPU core without any optimization, and FFT functions provided by the AMD Core Math Library (ACML) module were used [23]. The ACML has both single-processor and multiprocessor versions. The single-processor version of the ACML can be run on a multiprocessor machine. In our serial codes, we used the single-processor version of the ACML. Therefore, our code execution was completely serial.

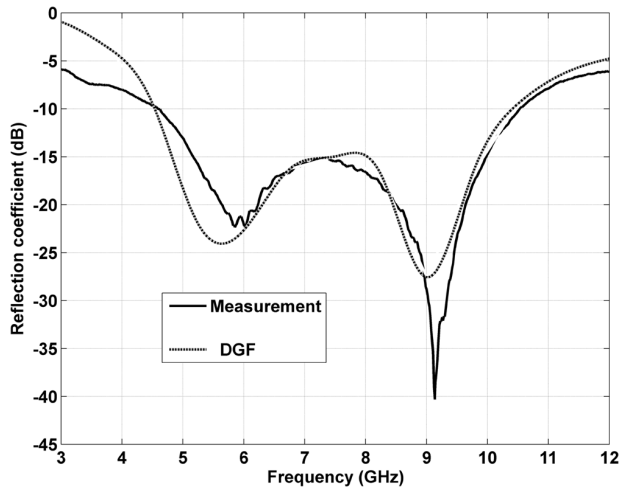

Fig. 13. Simulated and measured return loss of the antenna.

The memory usage for DGF calculation through the flowchart in Fig. 5(b) and through the FDTD method is dependent on the number of cells, which in turn is dependent on the window size. In both methods, the values associated with each cell are real numbers in double precision (8 bytes). In the proposed method, each cell has three values of magnetic vector potential and one value of scalar potential, which are related to their values at two previous time steps. This gives a memory usage of $2\times4\times8$ bytes per cell. However, each FDTD cell has six field values, which are related to their values at only one previous time step. This gives a memory usage of 6×8 bytes per FDTD cell. Therefore, the memory allocation in the proposed method is approximately 30 percent more than that in the FDTD method. However, as previously mentioned, the FDTD method for DGF extraction cannot estimate the steady-state values of DGFs correctly.

Since, for the given values of the Courant numbers, the DGFs are computed and stored once, and the current of different antennas can be computed through (35) using the stored DGFs, the computational runtime is separated into two parts: a time for generating DGFs and a time for computing the current from (35).

The time for generating the discrete dyadic Green's function is constant for various antenna sizes but is highly dependent on the window size. The larger the window size is, the bigger the number of cells will be, and the longer the computations will take. However, we have found by trial and error that the proper window size for this type of antenna is about 500 to 600. Fig. 14 shows the log-log diagram of the CPU time for generation of the required DGFs versus the window size. This time is dramatically reduced compared with the generation time for the closed-form-DGFs derived in [5].

The time for computing the current from (35) is strongly dependent on the size of the antenna, and most of this time is spent on calculating the time convolution of (35). As the electrical dimension of the antenna increases, the proposed method becomes

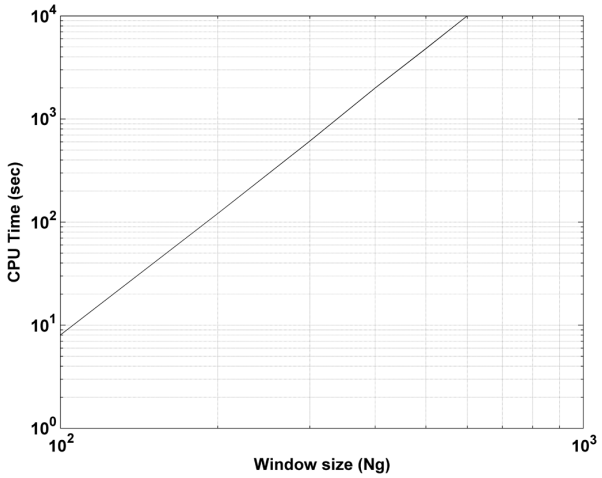

Fig. 14. CPU time for generation of the required DGFs.

TABLE III
COMPARISON OF THE TOTAL CPU TIME AND MEMORY REQUIRED FOR THE ANALYSIS OF THE ANTENNAS

Antenna	CPU Time (sec)		Memory (Mb)	
	DGF	FDTD	DGF	FDTD
Printed dipole	92	195	480	110
CPW-fed Monopole	1080	740	4300	350

inefficient. The calculations of the spatial convolutions of (35) are accelerated by using the FFT algorithm [22]. However, further investigations can be done on the use of other fast convolution algorithms in the time convolution calculation of (35). Because the window length of the time convolution of (35) is long (about 500 to 600 terms depending on the window size), an iterated convolution algorithm that decomposes a long convolution into several levels of short convolutions can be used. Table III presents a comparison of the CPU time and memory required for the calculation of update equations between the FDTD and the DGF method for a total of 3000 time steps. Note that Table III lists only the time needed for computing the current from (35) in DGF simulation since, for the analysis of each antenna, we can use stored DGFs, and it is not necessary to repeat the computation of the DGFs unless the Courant numbers change. As shown in the table, the update equation of the current in (35) for the DGF method in conjunction with the spatial FFT algorithm requires more memory because of the complex numbers involved in the calculations. A real-valued fast Fourier transform can alleviate this challenge. In addition, the savings in computational runtime that is offered by the DGF method depends on the size of the antenna.

IV. CONCLUSION

A new numerical technique for extraction of discrete Green's functions in multilayered media has been proposed. This method does not suffer from the implementation challenges of analytical closed-form-DGFs in free space. The steady-state of the DGFs is also predicted correctly, facilitating the use of the truncation window. Furthermore, the application of the method has been demonstrated by the analysis of two simple antennas. Despite the fact that the computations are done only on the antenna and absorbing boundary conditions are not used, this method has some limitations in the memory allocation and time convolution calculation for large antennas.

REFERENCES

[1] J. Vazquez and C. G. Parini, "Discrete Green's function formulation of FDTD method for electromagnetic modelling," *Electron. Lett.*, vol. 35, no. 7, pp. 554–555, Apr. 1999.
[2] J. Vazquez and C. G. Parini, "Antenna modelling using discrete Green's function formulation of FDTD method," *Electron. Lett.*, vol. 35, no. 13, pp. 1033–1034, Jun. 1999.
[3] W. Ma, M. R. Rayner, and C. G. Parini, "Discrete Green's function formulation of the FDTD method and its application in antenna modeling," *IEEE Trans. Antennas Propag.*, vol. 53, no. 1, pp. 339–364, Jan. 2005.
[4] R. Kastner, "A multidimensional Z-transform evaluation of the discrete finite difference time domain Green's function," *IEEE Trans. Antennas Propag.*, vol. 54, no. 4, pp. 1215–1222, Apr. 2006.
[5] S. K. Jeng, "An analytical expression for 3-D dyadic FDTD-compatible Green's function in infinite free space via z-transform and partial difference operators," *IEEE Trans. Antennas Propag.*, vol. 59, no. 4, pp. 1347–1355, Apr. 2011.
[6] R. Holtzman and R. Kastner, "The time-domain discrete Green's function method (GFM) characterizing the FDTD grid boundary," *IEEE Trans. Antennas Propag.*, vol. 49, no. 7, pp. 1079–1093, 2001.
[7] R. Holtzman, R. Kastner, E. Heyman, and R. W. Ziolkowski, "Stability analysis of the Green's function method (GFM) used as an ABC for arbitrarily shaped boundaries," *IEEE Trans. Antennas Propag.*, vol. 50, no. 7, pp. 1017–1029, 2002.
[8] R. Holtzman, R. Kastner, and E. HeymanR. W. Ziolkowski, "Ultra-wideband cylindrical antenna design using the Green's function method (GFM) as an absorbing condition (ABC) and the radiated field propagator in a genetic optimization," *Microw. Opt. Tech. Lett*, vol. 48, no. 2, pp. 348–354, 2006.
[9] T. P. Stefanski, "Applications of the discrete Green's function in the finite difference time domain method," *Progr. Electromagn. Res.*, vol. 139, pp. 479–498, 2013.
[10] S. Malevsky, E. Heyman, and R. Kastner, "Source decomposition as a diakoptic boundary condition in FDTD with reflecting external regions," *IEEE Trans. Antennas Propag.*, vol. 58, no. 11, pp. 3602–3609, 2010.
[11] A. Cottee, W. Ma, M. R. Rayner, and C. G. Parini, "Application of the DGF-FDTD technique to log periodic antennas," in *Proc. Int. Conf. on Antennas and Propagation*, U.K., Apr. 2003, pp. 553–556.
[12] W. Ma, M. R. Rayner, and C. G. Parini, "The modeling of a Yagi-Uda array antenna using the DGF-FDTD method," in *Proc. Int. Symp. on Antennas and Propagation*, USA, Jun. 2003, pp. 780–783.
[13] S. Mirhadi, M. Soleimani, and A. Abdolali, "UWB antennas analysis using FDTD-based discrete Green's function approach," *IEEE Antennas Wireless Propag. Lett.*, vol. 12, pp. 1089–1093, 2013.
[14] S. Mirhadi, M. Soleimani, and A. Abdolali, "Discrete Green's function approach for the analysis of a dual band-notched UWB antenna," *Microw. Opt. Tech. Lett*, vol. 55, no. 9, pp. 2168–2174, 2013.
[15] T. P. Stefanski, "Fast implementation of FDTD-compatible Green's function on multicore processor," *IEEE Antennas Wireless Propag. Lett.*, vol. 11, pp. 81–84, 2012.
[16] T. P. Stefanski, "Hybrid technique combing the FDTD method and its convolution formulation based on the discrete Green's function," *IEEE Antennas Wireless Propag. Lett.*, vol. 12, pp. 1448–1451, 2013.
[17] T. P. Stefanski, "Accuracy of the discrete Green's function formulation of the FDTD method," *IEEE Trans. Antennas Propag.*, vol. 61, no. 2, pp. 829–835, Feb. 2013.
[18] L. Tsang, C. J. Ong, C. C. Huang, and V. Jandhyala, "Evaluation of the Green's function for the mixed potential integral equation (MPIE) method in the time domain for layered media," *IEEE Trans. Antennas Propag.*, vol. 51, no. 7, pp. 1559–1571, Jul. 2003.
[19] M. J. Tsai, F. D. Flaviis, O. Forham, and N. G. Alexopoulos, "Modeling planar arbitrarily shaped microstrip elements in multilayered media," *IEEE Trans. Microw. Theory Tech.*, vol. 45, no. 3, pp. 330–337, Mar. 1997.
[20] F. Ling and J. M. Jin, "Efficient electromagnetic modeling of microstrip structures in multilayer media," *IEEE Trans. Microw. Theory Tech.*, vol. 47, no. 9, pp. 1810–1818, Sep. 1999.

[21] M. Vrancken and G. A. E. Vandenbosch, "Hybrid dyadic-mixed-potential and combined spectral-space domain integral equation analysis of quasi-3-D structures in stratified media," *IEEE Trans. Microw. Theory Tech.*, vol. 51, no. 1, pp. 216–225, Jun. 2003.
[22] S. Mirhadi, M. Soleimani, and A. Abdolali, "An FFT-based approach in acceleration of discrete Green's function method for antenna analysis," *Progr. Electromagn. Res. M*, vol. 29, pp. 17–28, 2013.
[23] AMD: AMD Core Math Library [Online]. Available: http://developer.amd.com/tools-and-sdks/cpu-development/amd-core-math-library-acml/

Salma Mirhadi received the B.Sc. degree from the Iran University of Science and Technology (IUST), Tehran, Iran, in 2006 and the M.Sc. degree from the K. N. Toosi University of Technology, Tehran, Iran, in 2009, both in electrical engineering. Since 2009, she has been working toward the Ph.D. degree in electrical engineering at IUST.

Mohammad Soleimani received the B.Sc. degree in electrical engineering from the University of Shiraz, Shiraz, Iran, in 1978 and the M.Sc. and Ph.D. degrees from Pierre and Marie Curio University, Paris, France, in 1981 and 1983, respectively.

He is a Professor at the Iran University of Sciences and Technology, Tehran, Iran. He has also served in many executive and research positions. He has authored and coauthored 19 books (in Persian) and more than 200 journal and conference papers. His research interests include electromagnetics, high-frequency electronics, and antennas.

Ali Abdolali was born in Tehran, Iran, in 1974. He received the B.Sc. degree from the University of Tehran, the M.Sc. degree from the University of Tarbiat Modares, Tehran, and the Ph.D. degree from the Iran University of Science and Technology (IUST), Tehran, Iran, all in electrical engineering, in 1998, 2000, and 2010, respectively.

In 2010, he joined the Department of Electrical Engineering, Iran University of Science and Technology, Tehran, Iran, where he is an Assistant Professor of electromagnetic engineering. His research interests include electromagnetic wave scattering, radar cross section (RCS), radar absorbing materials (RAM), EM Waves controlling, cloaking, metamaterials, EM Waves in complex media (anisotropic, inhomogeneous, dispersive media, metamaterials), frequency selective surfaces (FSS), bio-electromagnetism (BEM). He has authored or coauthored over 50 articles in international journals and conferences.